ADVANCED PROCESSING OF METALLIC POWDERS
FOR FOSSIL ENERGY APPLICATIONS

Iver E. Anderson
222 Metals Development, Ames Lab. (USDOE), Iowa State University, Ames, IA 50011
E-mail: andersoni@ameslab.gov; Telephone: (515) 294-9719; Fax: (515) 294-8727

David J. Byrd
109 Metals Development, Ames Lab. (USDOE), Iowa State University, Ames, IA 50011
E-mail: byrd@ameslab.gov; Telephone: (515) 294-5747; Fax: (515) 294-8727

Joel R. Rieken
223 Metals Development, Mater. Sci. & Eng., Iowa State University, Ames, IA 50011
E-mail: jrieken@iastate.edu; Telephone: (515) 294-1602; Fax: (515) 294-8727

Stephen N. Paglieri
Los Alamos National Laboratory; P.O. Box 1663, MS-C927; Los Alamos, NM 87545
E-mail: steve.paglieri@lanl.gov; Telephone: (505) 667-0652; Fax: (505) 665-1226

ABSTRACT

This project seeks to develop innovative methods and to enhance process control of metal powder production by gas atomization methods to benefit the implementation of several emerging Fossil Energy (FE) technologies that utilize metal powders of specific size ranges and types, which are not efficiently produced by industrial powder processing. A high efficiency gas atomization nozzle was used to maximize powder yields of ultrafine (dia. < 10 μm) powders to eliminate a major barrier to the use of new concepts for fabrication of hydrogen membranes, for example. A smooth micro-porous metallic support surface was developed with LANL for fabrication of robust hydrogen separation membranes from Pd alloy thin films, approximately 2μm thick, for advanced coal-fired power plants with CO_2 capture capability. Recent work involved sintering of a 75μm thick primary membrane support layer from ultrafine (<3μm dia.) gas-atomized spherical Fe-16Al-2Cr (wt.%) powder onto a coarse (40μm porosity) stainless steel frit as a secondary support. Crack-free membrane support surfaces with 0.1-0.5μm porosity resulted and a finished membrane achieved encouraging hydrogen separation performance. However, SEM and profilometry revealed some support surface irregularities, related to the coarse frit. New support surfaces were sintered on finer (10μm porosity) Inconel frits to overcome these defects. The results were characterized for surface roughness by SEM and AFM and for diffusion barrier formation by Auger spectroscopy, critical features for fabrication of successful Pd membranes. As an alternative to mechanical alloying for producing oxide dispersion strengthened (ODS) alloys for high temperature FE applications, Fe-Cr based powders encapsulated with a thin precursor oxide shell were produced by gas atomization reaction synthesis (GARS). Hot isostatic pressing (HIP) at 850C or 1300C fully consolidated the ODS precursor powder. The 1300C HIP and subsequent heat treatment promoted diffusion and exchange reactions that dissolved the trapped oxide shells and generated stable oxide nano-dispersoids in the microstructure. Results will be reported of the transformations that convert the Fe-(12.5-15.0)Cr-(0.15-1.0)Y (wt.%) powders to an isotropic ODS microstructure, including the effects of reduced oxygen and Ti additions on development of an ideal (fully transformed) microstructure. Heat-treated microstructures were analyzed by SEM and TEM. Changes in product phases were tracked with x-ray diffraction. High temperature tensile strength measurements assessed the effectiveness of the heat treatments.

INTRODUCTION

Free-standing porous filter sheets or tubes that were intended for the fly ash removal stage of hot gas cleanup have been fabricated using partial sintering of spherical powders of a Ni-16Cr-9Al-3Fe (wt.%) alloy that resists oxidation and corrosion by gaseous impurities commonly present in exhaust gas from the combustion of coal[1]. A critical characteristic of the high pressure gas atomized (HPGA) powders used for this work[2] was the thin oxide surface film on the as-atomized powders that permitted the diffusion process involved in forming the porous materials with strong sintered "neck" regions[1]. Alternative alloys with enhanced aluminum content such as Fe-16Al-2Cr are even more resistant to oxidation and corrosion by gaseous impurities (primarily SO_x) commonly present in exhaust gas from the combustion of coal, especially if protected by a "thermally grown" aluminum oxide layer on the surface that protects the bulk metal from oxidation and sulfur attack[3]. Because of the need for extremely long operational lifetime in such a corrosive atmosphere, Fe-16Al-2Cr alloy powders made by HPGA were chosen for the current study to serve as a new type of porous support surface (PSS) for a thin Pd alloy film to make an interstitial type of hydrogen selective composite membrane that can effectively separate high purity hydrogen from a hot (600-700C) synthesis gas input[4]. The interstitial separation concept involves rapid atomic diffusion through the Pd metal lattice structures and requires a porous (metallic) support surface with very low surface roughness as a support for effective physical vapor deposition (in a magnetron sputtering or electron beam evaporation system) of the continuous metal film[4]. The preferred pore size of the metallic support surface is very small, in the range of 0.1-0.5 μm, to help achieve the desired low surface roughness. To produce controlled porosity of this size range by loose powder sintering requires ultra-fine spherical powders of Fe-16Al-2Cr with dia. < 3 μm[5]. The deposition of a palladium film without defects depends on the ability to span all of the pores on the porous support surface[6]. Therefore, the critical qualities of a PSS for a palladium membrane are low surface roughness, small pore size, as mentioned above, as well as maximum pore population per unit area[7]. It is also most desirable to have a diffusion barrier phase at the interface between the PSS and the Pd membrane film (see Fig. 1). The purpose of the barrier is to inhibit diffusion of metallic atoms from the PSS, e.g., the Cr in stainless steel, into the palladium film, which causes a decrease in membrane permeability. Metallic interdiffusion that occurs between palladium and a PSS at temperatures ≥ 450°C has been reduced by thin layers of oxide, nitride, or refractory metal[8]. Of course, membrane performance stability then depends on the stability of the intermediate diffusion barrier layer.
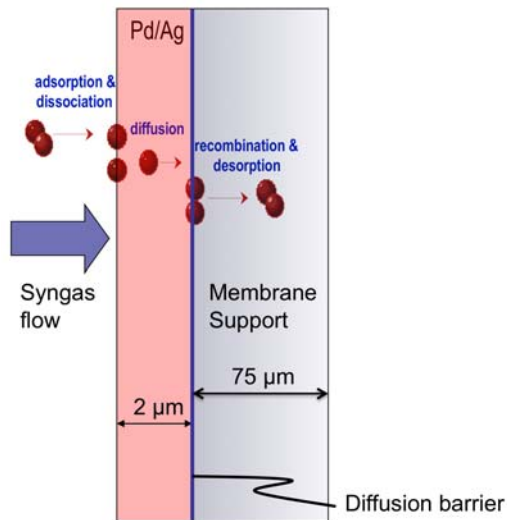

Figure 1. Schematic of the critical features of an improved hydrogen separation membrane of the interstitial type showing the direction of synthetic (mixed) gas flow.

Previous work by the co-authors had attempted to fabricate a freestanding thin wafer form of a porous substrate surface from dia. < 3μm powders of Fe-16Al-2Cr (wt.%) powders and had achieved a sufficient sintered state in this wafer structure to achieve the proper degree of open porosity[9]. However, a problem was encountered with mechanical integrity of the porous wafers, due to sintering shrinkage while supported on a bed of loose high purity alumina particles. These problems with wafer cracking prevented welding of the PSS to a coupling tube and the deposition of a Pd film to permit testing of the full membrane for hydrogen permeation. Thus, the continued work demanded the development of a new fabrication procedure for the Pd membrane porous support layer. Analysis of the cracking problems during sintering of the free-standing porous wafers lead to development of a new approach that uses a secondary support frit underneath the membrane support to add some mechanical interlocking and structural stiffness[5,10]. The frit and the PSS layer are contained inside of an Inconel tube to permit weld sealing of the Pd film periphery, if needed, and simple coupling to the flow test apparatus. A further improvement of the design of the sample configuration involved the cutting of a 3° (from horizontal) chamfer in the flat end of the tube to allow radial sintering shrinkage of the ultrafine powder layer to be accommodated by sliding along the chamfered surface without building tensile stresses. Results showed[5,10] that the sliding mechanism worked as intended, where a short length of separation appeared along the lower region of the chamfer, but the majority of this inclined surface, closer to the outer edge, was sealed well and the full layer was maintained in a crack-free condition. Following analysis of additional experimental results[5], it was concluded that a future improved sample configuration should substitute an alloy frit with a significantly finer average pore size, where 10 μm was selected.

Many of the inherent qualities of ferritic stainless steels, i.e. high thermal conductivity, high creep resistance, and low thermal expansion (low void swelling during neutron irradiation) distinguish them as a prominent choice for many applications in fossil-fueled power plants, as well as for cladding material in fission and fusion reactors[11]. However, traditional ferritic stainless steels lack the high temperature strength required for future generation systems[12]. To resolve this issue much work has been done to develop the use of nano-metric oxide particles as strengthening agents within the ferritic matrix[13]. Improved dispersoids have become more effective in impeding dislocation movement and minimizing grain boundary slip, thus increasing the strength of the alloy[14]. Most of the fabrication approaches for ODS ferritic stainless steels employ a mechanical alloying (MA) technique to generate the precursor particulate. The MA technique is currently used to create an ODS microstructure that can increase the elevated temperature mechanical properties of ferritic stainless steel alloys. However, this mechanical alloying process has several drawbacks that were recently highlighted in a review article entitled "Recent Developments in Irradiation-Resistant Steels" (G.R. Odette, et al)[15]. The article states that the practical development of nanodispersion-strengthened iron-based alloys faces some specific challenges including, the high cost of mechanically alloyed powder-consolidated materials compared with the cost for melt-processed alloys, the isotropic microstructure that arises from mechanical alloying, and the batch-to-batch variability in mechanical alloying. These challenges provide motivation for further research into new processing methods for the production of ODS ferritic stainless steel alloys.

To respond to this need, an innovative processing method, involving gas atomization reaction synthesis (GARS)[16], has been developed for the fabrication of precursor ODS ferritic stainless steel powder. During this process[17] each individual powder particle is coated in situ with a thin oxide shell during rapid solidification. The oxide shell is later used as an oxygen reservoir for the formation of nano-metric yttrium-enriched oxide dispersoids during high temperature isostatic consolidation. This paper will evaluate the consolidated microstructure evolution resulting from this new atomization processing technique, and will compare initial as-consolidated tensile

properties with data on commercially produced MA ODS ferritic stainless steel alloys. The results demonstrate the potential benefits of the GARS processing method for the formation of precursor powders for ODS ferritic stainless steel.

EXPERIMENTAL PROCEDURE

Powders of an iron aluminide alloy, Fe-16Al-2Cr (wt.%), were produced[18] with a high-pressure gas atomization (HPGA) system[2] to use in the current sintering experiments to make porous membrane support surfaces. A full set of ASTM screens with opening sizes below 140 mesh and down to 635 mesh (20μm) were used to obtain an estimate of the particle size distribution[2]. A portion of the < 20μm dia. powder was pneumatically classified (AccuCut, Donaldson, Inc.) to < 3μm dia. for the sintering experiments. To implement the new sample fabrication approach, the frit and PSS layer was designed to fit within a 9.6 mm O.D. x 6.4 mm I.D. x 2 cm length alloy (Inconel 600) tube that was counter-bored to accept a 316L stainless steel frit (40 μm avg. pore size) that was press fit from one end (into the enlarged bore). Later work used Inconel 600 alloy frit and tube materials, where the average pore size was 10 μm. The exterior surface of the frit was set into the end face (either flat or chamfered) of the tube by about 75 μm to provide a recessed mold cavity for slurry "casting" of the ultra-fine (dia.<3μm) powder of Fe-16Al-2Cr. In the slurry casting operation, the < 3 μm dia. powder was blended with methanol and poured onto the recessed mold cavity, followed by immediate "striking-off" of the surface with a planar (razor) blade or glass slide edge to produce a reasonably flat powder surface. Evaporation of the residual methanol was performed at ambient temperature in air, until the surface appeared dry. Each sample was vacuum (10⁻⁶ torr) sintered at 975C for times of 1-4 hours, based on previous work[6]. Later sintering work was performed in an alternative (smaller volume) vacuum furnace with thermocouple placement that permitted more accurate sample temperature sensing. Thus, sintering temperatures of 975, 850, and 825C were used, all for 1 hour. Optical microscopy and SEM of the sintered surface and a mounted and polished cross-section (unetched) of each sample provided initial characterization of the sintering results.

The precursor powder[19] for the ODS alloys was produced[18] using GARS with a reactive gas mixture of Ar and O_2. The reaction parameters (i.e., reactive gas content and inlet position) and the nominal chemical composition of each alloy are displayed below in Table 1. The resulting powders were collected and sieved into a selected size range (i.e., -20μm, 20-53μm, and +53μm) to be used for consolidation. The bulk oxygen content of the as-atomized powder particles was measured using an inert gas fusion (LECO) analyzer and the composition of each alloy was verified using inductively coupled plasma / atomic emission spectroscopy (ICP-AES).

Table 1. Nominal alloy composition (wt.%) and atomization processing parameters

Alloy	Fe (wt.%)	Cr (wt.%)	Y (wt.%)	Ti (wt.%)	Gas Content (vol.%)	Gas Inlet Position
CR-96	Bal.	12.5	1.0	-	Ar-5.0O_2	First Halo
CR-112	Bal.	15.0	0.5	-	Ar-0.5O_2	Nozzle
CR-118	Bal.	15.0	0.5	0.54	Ar-0.5O_2	Nozzle

The as-atomized powder particles, ranging from 20-53μm, were consolidated using hot isostatic pressing (HIP). The powder particles were laser welded under vacuum (10⁻⁷ torr) in a 316 stainless steel can. The consolidation temperature was 850°C (1562°F) or 1300°C (2372°F) at a pressure of 303 MPa (44 ksi) for a duration of 4.0 hours.

A mechanical testing system (MTS 810) with a high temperature resistance (657.01 HT) furnace was used to examine the tensile strength of the alloys. The tests were performed at 21°C, 400°C, 600°C, and 700°C (CR-96 was not tested at 700°C) in open air. The alloys were tested in the as-consolidated (i.e., 1300°C HIP) condition. The test procedure was based on the standard test methods for tension testing of metallic materials (ASTM-E 21-05) with a displacement rate of 0.1mm/min. The test specimens were secured in Inconel 718 threaded grips to provide sufficient high temperature capacity. The true stress was used in determining the tensile strength of the alloys. Microstructure analysis of the as-consolidated alloys and failure analysis of the fractured tensile specimens were conducting using a Hitachi S-2460N scanning electron microscope (SEM) with energy dispersive spectroscopy (EDS). The cross-sectional samples were ground flat using 400, 600, 1000, and 1200 silicon carbide grit paper and, subsequently, polished using 6.0, 1.0, and 0.25μm diamond pastes. The nano-metric dispersoids, in the as-consolidated (i.e. 1300°C HIP) condition, were preliminarily characterized using a Tecnai G^2 F20 scanning transmission electron microscope (STEM) at 200 keV. The chemical composition of the nano-metric dispersoids was imaged using a high angle annular dark field detector at a 15° α-tilt and measured using an energy dispersive x-ray detector. The nano-metric dispersoids found within the failed tensile specimens were imaged using a bright field detector. The STEM samples were ground flat using 400, 600, and 1000 silicon carbide grit paper, and polished using 6.0 and 1.0μm diamond pastes to a thickness and approximately 50μm. The samples were dimpled to a thickness of approximately 20μm and argon ion milled at 5kV and 1.0 mA until light penetration was detected. High-energy X-ray diffraction using synchrotron radiation at the Advanced Photon Source, Argonne national laboratory, was used for initial phase analysis of the yttrium-enriched dispersoids. The samples were tested in the as-consolidated (i.e., 1300°C HIP) condition at room temperature (CR-96 was not tested). A cylindrical specimen test geometry was used of 12.5mm height x 1.0mm diameter. The specimens were exposed at 10 sec. time intervals and a CCD detector was used for data collection.

RESULTS AND DISCUSSION

Along with the plan to use a frit material with 10μm pore size, a decision was also made to use an alloy, Inconel 600, that matched the alloy composition of the exterior tube and this type of frit was located. Thus, with this new sample material combination and the same sample geometry as the previous experiments above[5], following preparation of the smooth surface deposit of Fe-16Al-2Cr, sintering conditions for this sample were set to duplicate the previous choice of 975C for 1h under a high vacuum (approximately 1 X 10^{-6} torr). Due to an equipment problem, instead of the large volume furnace with a top-central (fairly remote) thermocouple, a smaller furnace with a very close-mounted thermocouple had to be utilized for this initial experiment with the new frit material. Therefore, because the frit composition was different and the actual sintering temperature may have been different, it was a challenge to understand why the wide "mud crack" pattern appeared upon examination of the post-sintered sample, as shown in Fig. 2a.

As a general explanation, it was thought that excess constraint, perhaps over a wide area, was operating against the sintering shrinkage, similar to that which caused the initial centerline cracking seen previously[5]. As an encouraging observation, circumferential cracking was not seen[5], presumably due the continued use of the 3° chamfer on the tube edge. One possible difference between the wide mud cracked results (see Fig. 2b and c) and the previous promising results[5] was the lack of good matching between the top surface of the new frit and the inner edge of the chamfered tube. It was possible that the mud cracks were due to excess constraint on the transforming powder layer due to the indented top surface of the frit that "anchors" the (shrinking) layer during sintering, generating wide spread tensile stress across the surface. Since it was possible that the tool (perhaps a tube) used to press the frit into position caused the

indented top surface, it was decided to remove and invert the frit piece in the tube for the next sintering experiment to improve the flatness of the frit and the matching of the inner edge of the tube with the frit.

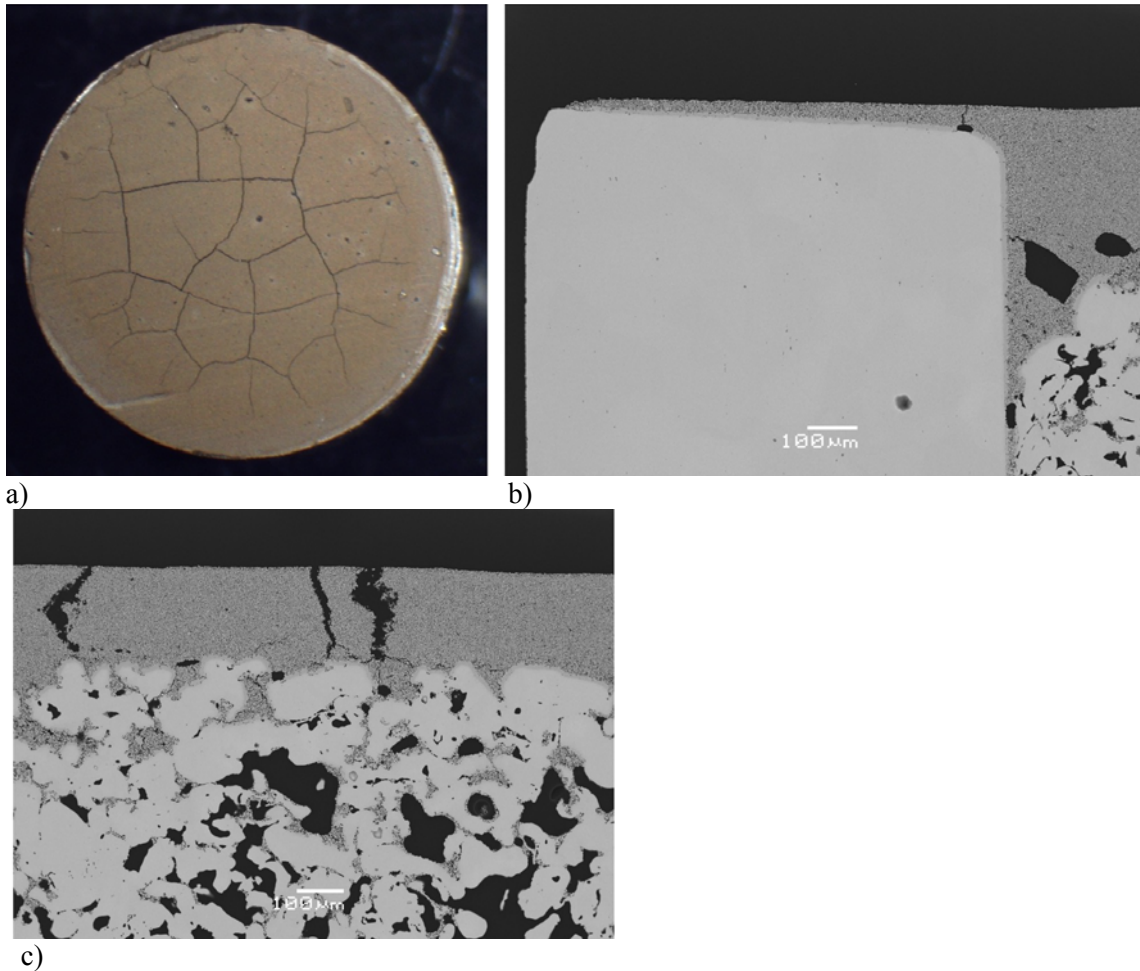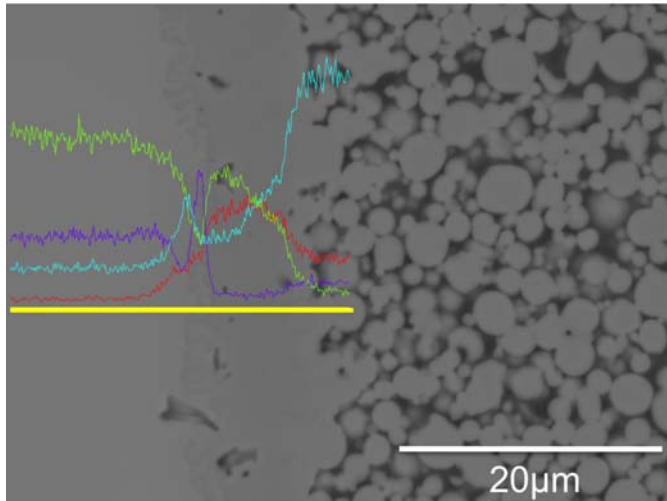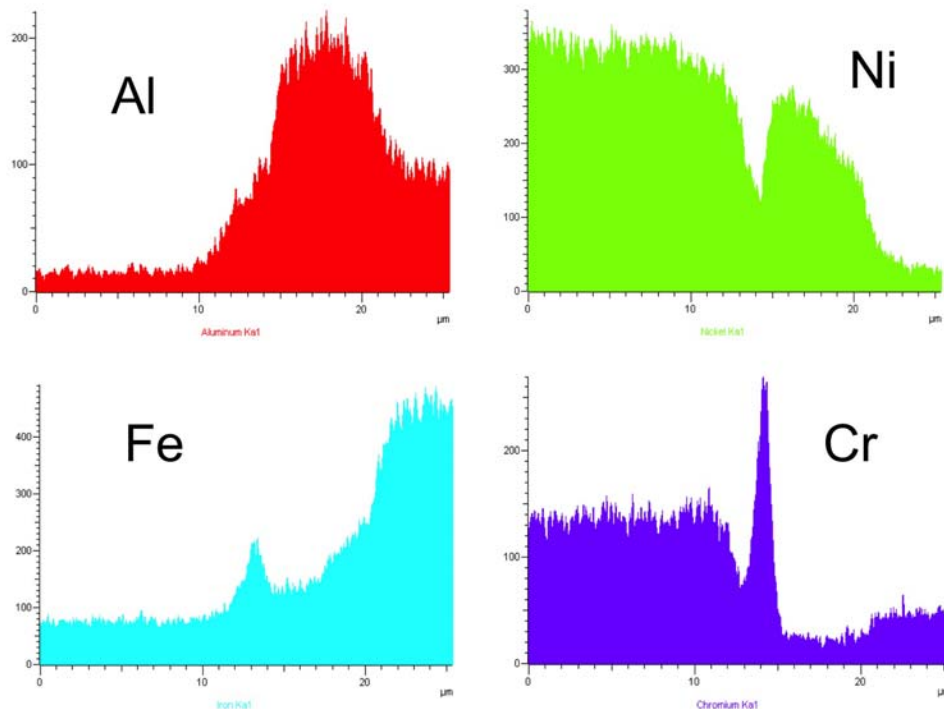a)   b)

c)

Figure 2. This presents, a) an optical micrograph of the severely mud cracked surface of the membrane support layer, b) a cross-section SEM micrograph of the chamfered tube region, and c) SEM micrograph of the central powder layer region showing the mud cracks in cross-section and the powder/frit interface reaction layer.

Another observation from the cross-section SEM micrographs Fig. 2 was an apparent reaction layer that formed during sintering between the Fe-16Al-2Cr powder and the Inconel 600 frit (see Fig. 2c). This type of reaction layer was not seen at the Fe-16Al-2Cr powder/316L frit interface in the previous (more promising) experiment[5]. On the other hand, approximately the same reaction layer can be seen after sintering between the Inconel 600 tube and the Fe-16Al-2Cr powder in both Fig 2b and the previous experiment[5]. Thus it was deduced that the reaction layer at the powder/frit interface was the more important contribution to excess constraint (and tensile stress) and must have promoted the pronounced mud cracking. A more detailed analysis of the Fe-16Al-2Cr/Inconel 600 reaction layer was conducted with energy dispersive spectroscopy (EDS) on the SEM, as shown in Fig. 3. As Fig. 3a indicates, a wide (10-15μm) reaction zone formed at the interface between the tube and the powder. Comparison of the intensity levels of the 4 elements (Ni, Al, Cr, and Fe) suggests that nickel aluminide phase formation has occurred at the immediate contact region between the powder and the tube and that a layer of Fe and Cr

enrichment is located in the subsurface region of the tube (see Figs. 3a and b). Thus, in an attempt to minimize the bonding effect of the nickel aluminide reaction at the powder/frit interface and its contribution to mud cracking, it was decided to significantly reduce the sintering temperature, from 975C to 850C (in the same small volume vacuum sintering furnace) in the next sintering experiment.

a)

b)

Figure 3. Summary of the results of EDS line scan analysis of the path (heavy yellow line) shown in a) SEM micrograph of the powder/tube reaction layer interface, and b) results for approximate concentration of each labeled element along the scan line.

Optical microscopy of the sample surface from the reduced sintering temperature (850C) experiment showed that only superficial surface mud cracks remained (see arrows in Fig. 4a), a significant improvement over the previous result in Fig. 2a. The cross-section SEM micrograph

in Fig 4c shows that the width of the mud cracks at the surface was less than about 5-10 µm, but was still too wide to be acceptable for full coverage by a PVD layer of Pd. Also, Fig. 4b reveals that the outer edge of the frit was still depressed at the tube interface, perhaps by disruption of the frit surface during press fitting by the obvious projection on the inner edge of the tube, in spite of attempts to invert the frit and to improve the matching with the tube. Actually, it is interesting to see (in Fig. 4b) the trail of porosity that extends from the chamfered surface of the tube into the partially sintered powder layer, perhaps marking the (preferred) "glide path" of powder disruption (shrinkage contraction) during sintering. Closer examination of the powder/tube and powder/frit interfaces (see Figs. 4b and c) with SEM and EDS scans (not shown) revealed that the thickness of the (nickel aluminide, verified by EDS) reaction layer was reduced to less than about 5µm, probably due to the significantly reduced sintering temperature. Unfortunately, the reaction layer still appeared to exert sufficient bonding constraint to the powder layer to help promote the slight mud cracking effect. Thus, the next sintering experiment was planned for an even lower temperature, 825C, to further diminish the powder/frit bonding, while taking more care with the tube interior surface finish and the frit insertion process. A key challenge for the next experiment was to determine if sufficient interparticle bonding (sinter "tacking") would remain to hold the Fe-16Al-2Cr powder layer together for sample handling purposes.

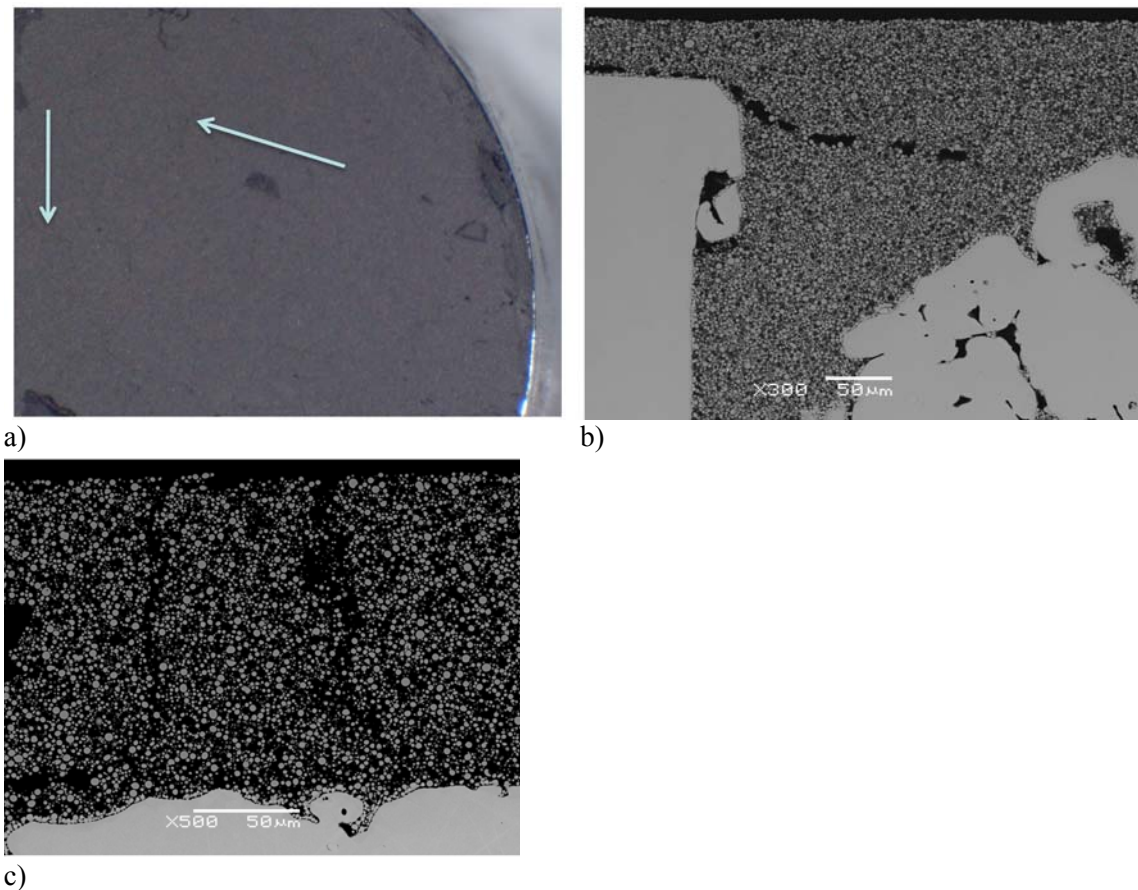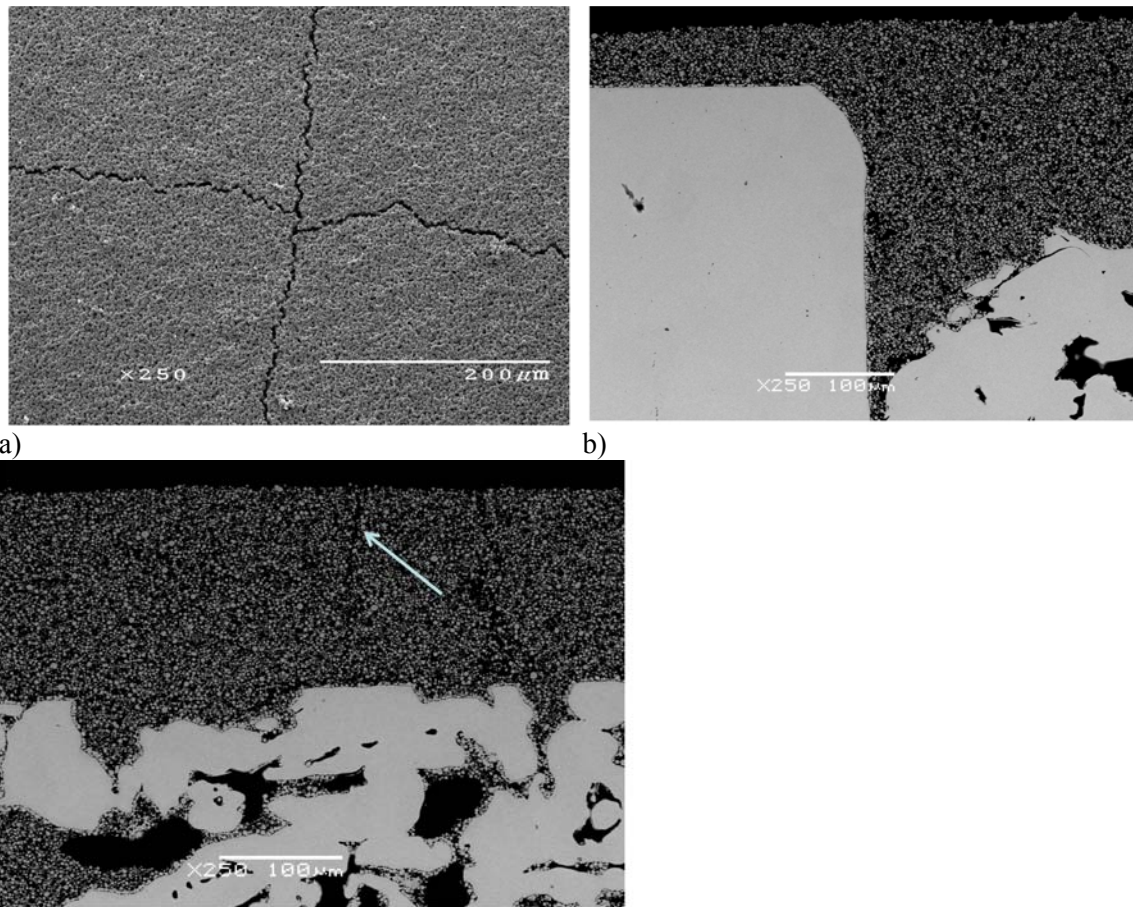a)   b)

c)

Figure 4. This presents, a) an optical micrograph of the superficial mud cracks (examples indicated by arrows) on the membrane support layer surface, b) a cross-section SEM micrograph of the chamfered tube region, and c) SEM micrograph of the central powder layer region showing narrow mud cracks in cross-section that extend from the top of the image.
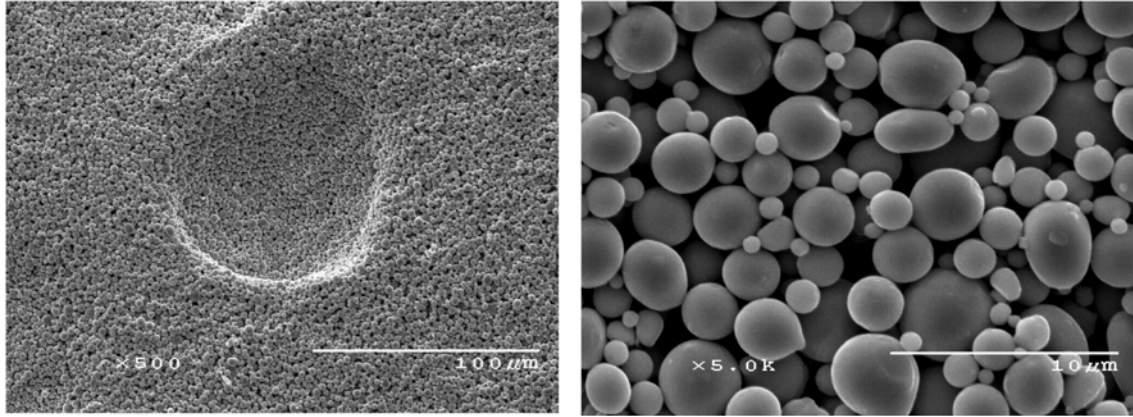
At the lowest temperature sintering conditions (825C, 1h), SEM was needed to clearly show (see Fig. 5a) that some "micro" mud cracks still remained in the surface of the powder layer. As Fig.

5c indicates, the width of the cracks was probably only about one particle wide and could be bridged (perhaps) during PVD deposition of the Pd film. Also, as Fig. 5b shows, the interior tube edge was finished better, but frit next to the tube wall was still depressed, probably due to unavoidable abrasion and frit disintegration due to the press fit condition. Unfortunately, as before, this lack of matching of the frit surface with the chamfered tube edge still would contribute to constraint and tensile stress on the powder layer during sintering. To eliminate this frit damage situation in future sintering experiments, the frit diameter will be selected to merely slide into the tube interior, not as a press fit condition that requires force for insertion.

a)   b)

c)

Figure 5. This presents, a) SEM micrograph of the "micro" mud cracks on the membrane support layer surface, b) a cross-section SEM micrograph of the chamfered tube region, and c) SEM micrograph of the central powder layer region showing "micro" mud cracks in cross-section that extend from the top of the image (arrow points to example).

Because of uncertainty about the ability to sufficiently sinter the Fe-16Al-2Cr powders at only 825C, the as-sintered substrate sample was inverted and impacted (by hand, indirectly) to free any un-bonded particles. Fig. 6 shows that, as suspected, the reduced sintering temperature resulted in an occasional complete lack of sinter tacking in local regions of the powder surface layer, giving rise to concave "divots" on the surface, as given in Fig. 6a. Fig. 6b provides confirmation of insufficient sintering, since obvious visual evidence of neck formation appears to be lacking, even between the smallest particles. Apparently, an increased sintering temperature is needed for improved interparticle bonding in future sintering experiments.

a)   b)

Figure 6. SEM micrographs of a) a surface divot that resulted from release of unbonded particles, and b) view of as-sintered surface showing no obvious sintered neck formation.

Interestingly, although the lack of sintering between particles of Fe-16Al-2Cr was noted at the 825C sintering temperature, the SEM micrograph of Fig. 7 shows that the nickel aluminide (exothermic) formation reaction at the powder/frit interface cannot be suppressed completely, even at this relatively low temperature. Thus, the resulting bond between the stationary frit and the shrinking powder layer still contributes to excess tensile stress on the sintering powder layer. In light of these results, it was decided that future PSS sintering experiments should use a 316L stainless steel frit to eliminate strong bonding at the powder/frit interface, similar to the previous promising results[5]. However, the stainless steel frit will be obtained with a 10µm pore size to retain the advantage of resistance to sink hole formation.
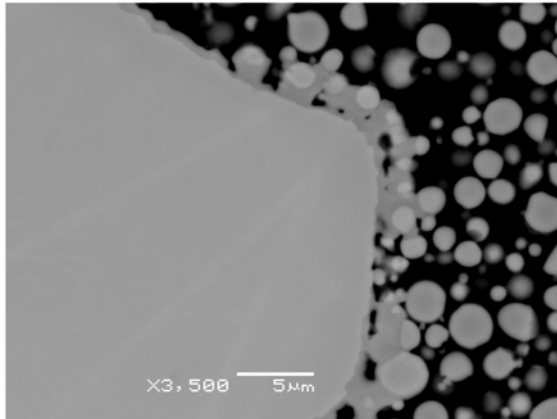

Figure 7. SEM micrograph of the powder/frit particle interface after sintering at 825 for 1h, showing evidence for a minor level of interfacial reaction.

The chemical composition of the as-atomized ODS precursor powder is shown below in Table 2. During the melting and super heating process required for close coupled gas atomization various amounts of the alloying constituents were reduced. Generally, the chromium loss was inconsequential and was measured to be less than a 2.0 wt.% change. The yttrium loss during atomization was more significant and varied with alloy. The weight percent loss of yttrium for the alloy CR-96, CR-112, and CR-118 was 33.0 wt.%, 70.0 wt.%, and 36.0 wt.% respectively.

Table 2.   As-atomized alloy chemical composition

Alloy	Fe (wt.%)	Cr (wt.%)	Y (wt.%)	Ti (wt.%)	O (wt.%)
CR-96	Bal.	12.44	0.67	-	.08
CR-112	Bal.	14.72	0.15	-	0.4
CR-118	Bal.	14.90	0.32	0.43	0.4

The surface chemistry of the as-atomized powder particles for the three chemical reservoir (CR) alloys was analyzed using Auger electron spectroscopy (AES) depth profiling. The sputtering rate was 10nm per minute based on a SiO_2 standard using 3 keV Ar ions. The AES depth profiles for each alloy are shown in Figure 8. The AES surface analysis of alloy CR-96 showed elevated intensities of oxygen and yttrium at the powder particle surface indicative of a yttrium oxide scale with a thickness of approximately 23nm. The AES surface analysis of alloy CR-112 revealed an enrichment of chromium and oxygen at the surface of the powder particles indicative of a chromium oxide scale with a thickness of approximately 112nm. The AES surface analysis of alloy CR-118 also revealed an enrichment of chromium and oxygen at the surface of the powder particles suggesting a chromium oxide scale with a thickness of approximately 125nm.
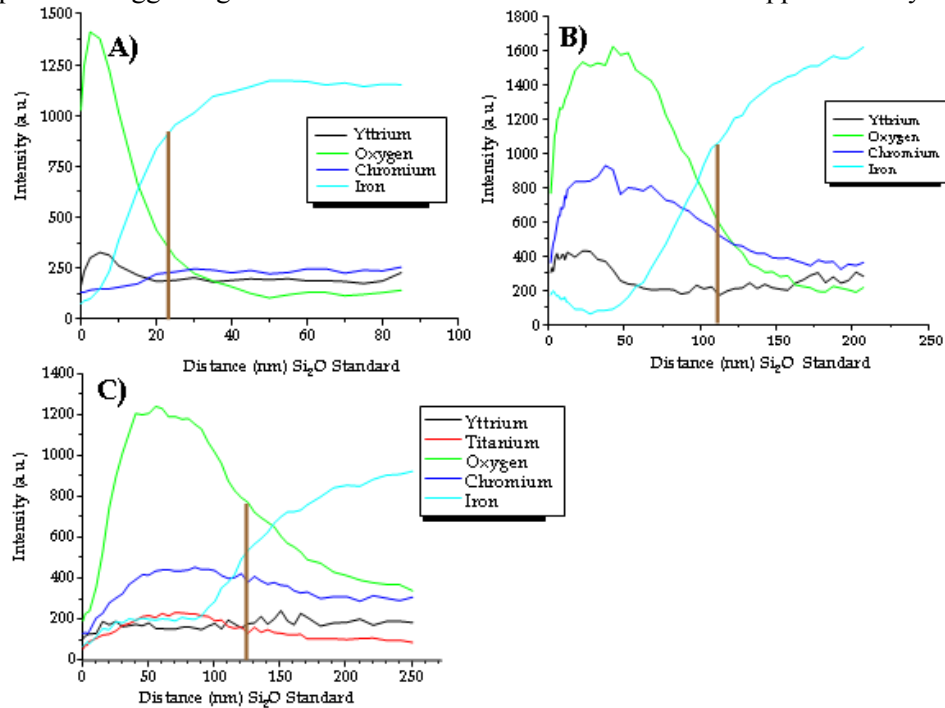

Figure 8. Auger electron spectroscopy (AES) depth profiles A) CR-96, B) CR-112, and C) CR-118.

The 850°C as-HIPped microstructure was examined using SEM with backscattered electron imaging (BEI), as shown in Fig. 9. Alloy CR-96 had no detectable prior particle boundaries (PPB's) at lower magnifications (e.g., 500X), but at higher magnifications (e.g., 5,000X) small chemical micro-segregation regions were detected. These regions were identified to be yttrium-enriched using energy dispersive spectroscopy. Alloy CR-112 had 2.52 vol.% of residual intact PPB oxide with an average bi-layer thickness of 223nm. The PPB oxide was identified to be chromium (III) oxide (Cr_2O_3) using wavelength dispersive spectroscopy (WDS). Alloy CR-118 had 2.22 vol.% of residual intact PPB oxide with an average bi-layer thickness of 254nm. This oxide was identified to be titanium (II) oxide (TiO) using WDS.
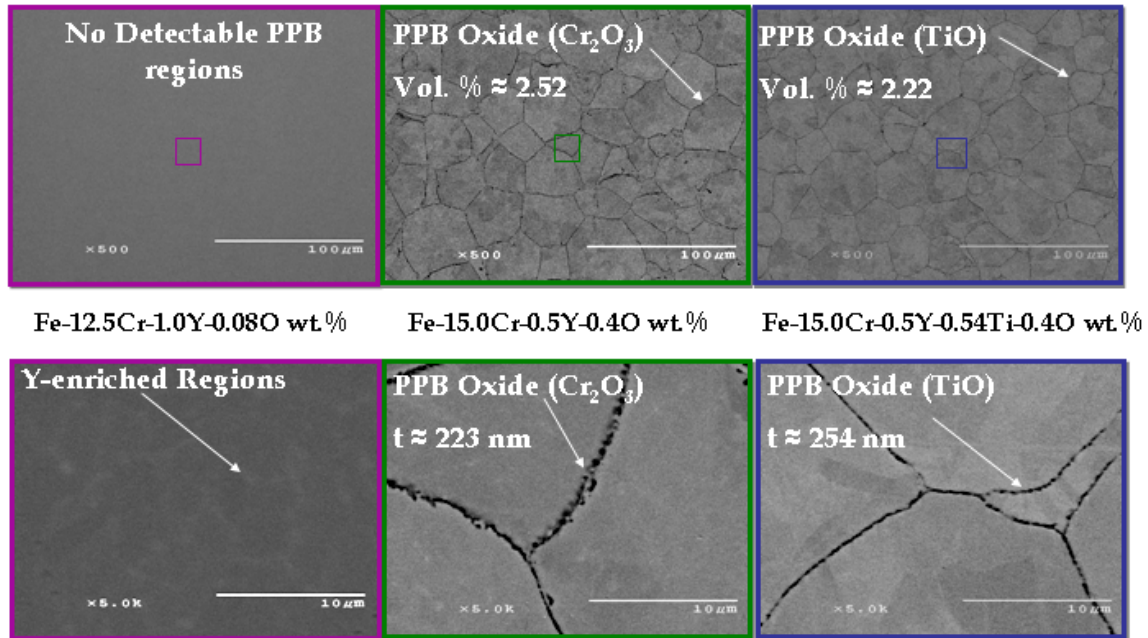
Figure 9. Low temperature HIPped (i.e. 850°C) microstructures of alloy CR-96 (purple), CR-112 (green), and CR-118 (blue).

The 1300°C as-HIPped microstructure was also examined using a SEM with a BEI detector. The reacted alloy microstructures resulting from elevated temperature consolidation are shown in Figure 10.
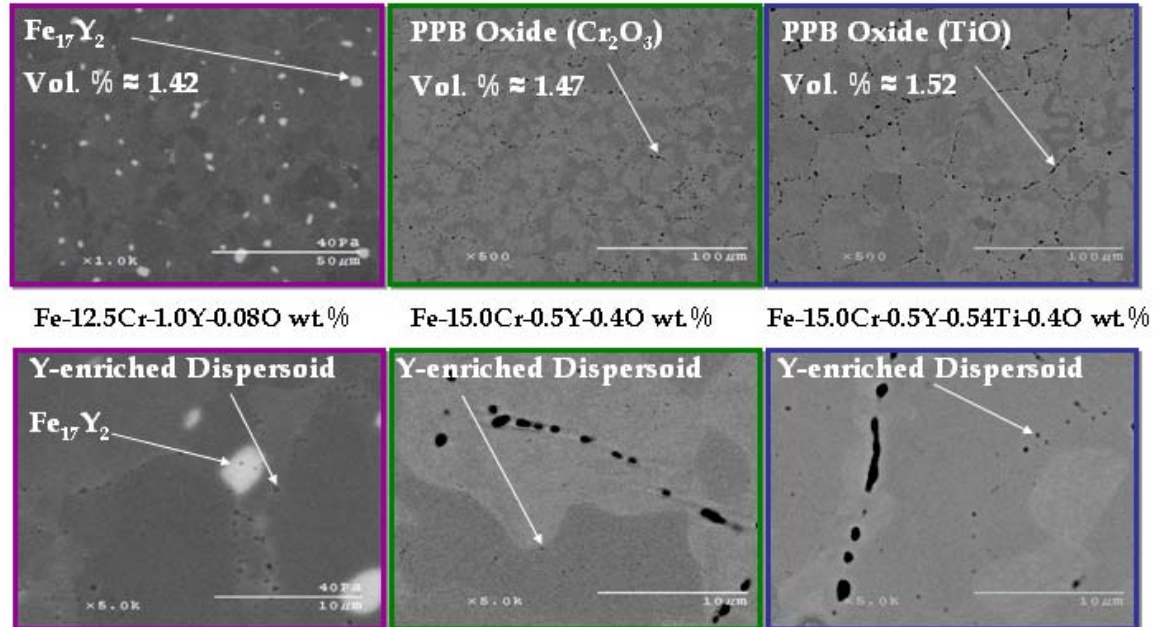

Figure 10. 1300°C as-HIP microstructures for alloy CR-96 (purple), CR-112 (green), and CR-118 (blue).

The microstructure of alloy CR-96 was significantly altered during the elevated temperature HIP process. The precipitation of an iron-yttrium intermetallic phase ($Fe_{17}Y_2$) with a 1.42 vol.% was detected. In addition, at higher magnifications small (less than 1.0μm) yttrium-enriched

dispersoids were identified. Alloy CR-112 demonstrated a considerable change in microstructure with the dissociation of 1.07 vol.% Cr_2O_3. At higher magnifications a clear break-up of the PPB Cr_2O_3 was observed with the formation of small (less than 1.0µm) yttrium-enriched dispersoids. Alloy CR-118 showed a substantial change in microstructure with the dissociation of 0.7 vol.% TiO. At higher magnifications a clear break-up of the PPB TiO was observed with the formation of small (less than 1.0µm) yttrium-enriched dispersoids.

Phase analysis of the 1300°C as-HIPped microstructure for alloys CR-112 and CR-118 was evaluated using high energy synchrotron X-ray radiation. The resulting x-ray patterns for the two alloys are shown in Figure 11.
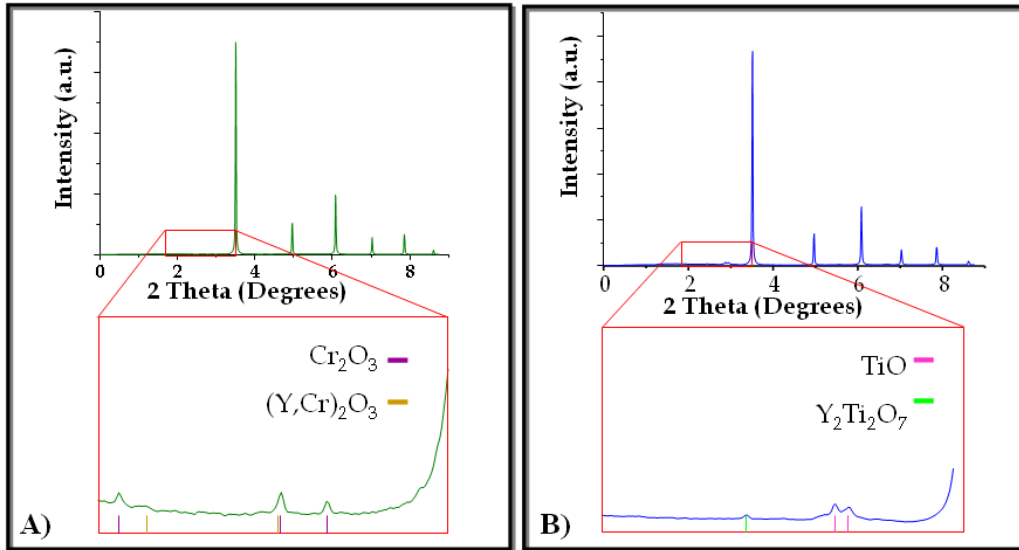

Figure 11. As-consolidated (i.e. 1300°C HIP) synchrotron X-ray diffraction patterns A) CR-112 and B) CR-1118.

The X-ray pattern of CR-112 identified the primary phase as α-Fe (i.e., matrix phase) and the secondary phase to be Cr_2O_3 (i.e., PPB oxide), but was unsuccessful in fully identifying the yttrium-enriched oxide dispersoid phase. The X-ray pattern of CR-118 identified the primary phase as α-Fe (i.e., matrix phase) and two secondary phases. The two secondary phases were TiO (i.e., PPB oxide) and yttrium titinate ($Y_2Ti_2O_7$). Full phase refinement of the secondary phases was not completed, and phase identification was assigned using peak position matching (of the most intense peaks) from the literature[20-23].

STEM with EDS capabilities was used to evaluate the chemical composition of the yttrium-enriched dispersoid phase found in the high temperature (i.e., 1300°C) HIPped alloys. Larger dispersoids that were of a similar size to those detected in the SEM were chosen for chemical analysis. The EDS chemical analysis results are displayed in Figure 12.
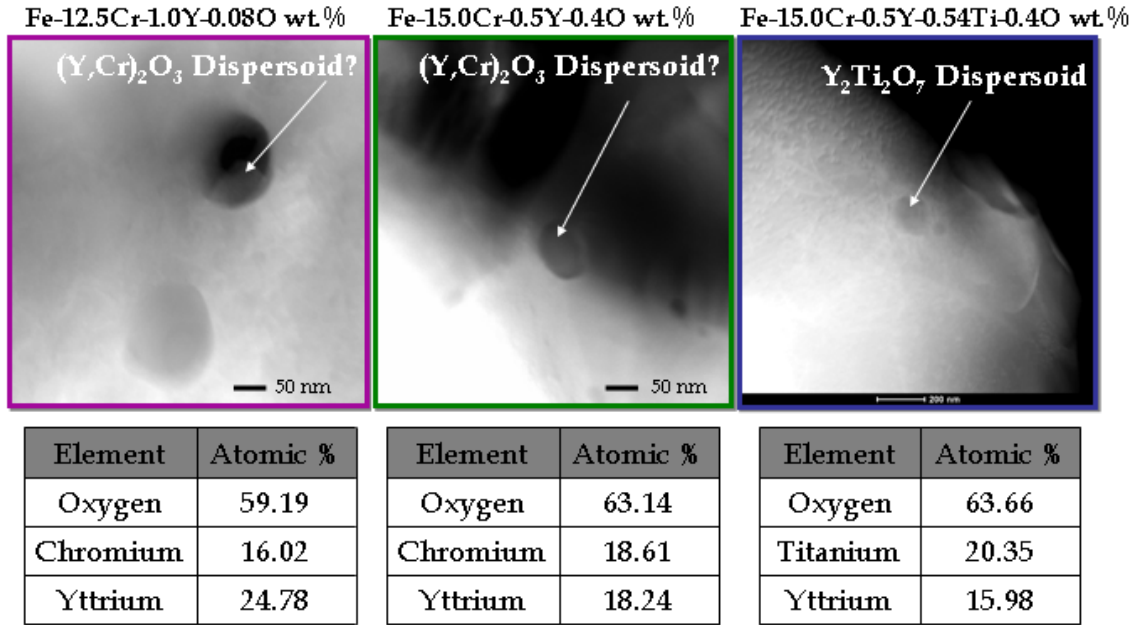
Figure 12. STEM images highlighting the analyzed dispersoids with EDS results listed below the corresponding image for alloy CR-96 (purple), CR-112 (green), and CR-118 (blue).

The EDS results for the dispersoids analyzed in alloy CR-96 identified oxygen, chromium, and yttrium with atomic percentages of 59.19, 16.02, and 24.78 respectively. The approximate ratio of metal to oxygen in the analyzed dispersoids is 0.689, which based on chemical components could be rationalized to represent yttrium-chrome oxide $((Y,Cr)_2O_3)$ when analytical measuring errors are taken into consideration. The chemical composition results for the dispersoids analyzed in alloy CR-112 identified oxygen, chromium, and yttrium with atomic percentages of 63.14, 18.61, and 18.24 respectively. The approximate ratio of metal to oxygen in the analyzed dispersoids is 0.583, which based on chemical components could again be rationalized to represent yttrium-chrome oxide $((Y,Cr)_2O_3)$ when analytical measuring errors are taken into consideration. The EDS results for the dispersoids analyzed in alloy CR-118 identified oxygen, titanium, and yttrium with atomic percentages of 63.66, 20.36, and 15.98 respectively. The approximate ratio of metal to oxygen in the analyzed dispersoids is 0.571, which based on chemical components could be rationalized to represent yttrium titinate $(Y_2Ti_2O_7)$ when analytical measuring errors are taken into consideration.

The tensile strengths of alloys CR-96, CR-112, and CR-118 were tested at 21°C, 400°C, 600°C, and 700°C (CR-96 was not tested at 700°C). Finite element analysis (FEA) calculations ensured that all localized plastic strain (i.e., necking) would occur in the gauge length of the cylindrical tensile bars[19]. A summary of resulting ultimate tensile strength values was compared with results from three commercial mechanically alloyed (MA) Fe-based ODS systems in Figure 13. The three alloys used for comparison were MA-956, MA-957, and PM 2000 that were tested longitudinal to their final deformation direction (in the strongest direction) and the data was taken from the literature[24-26].
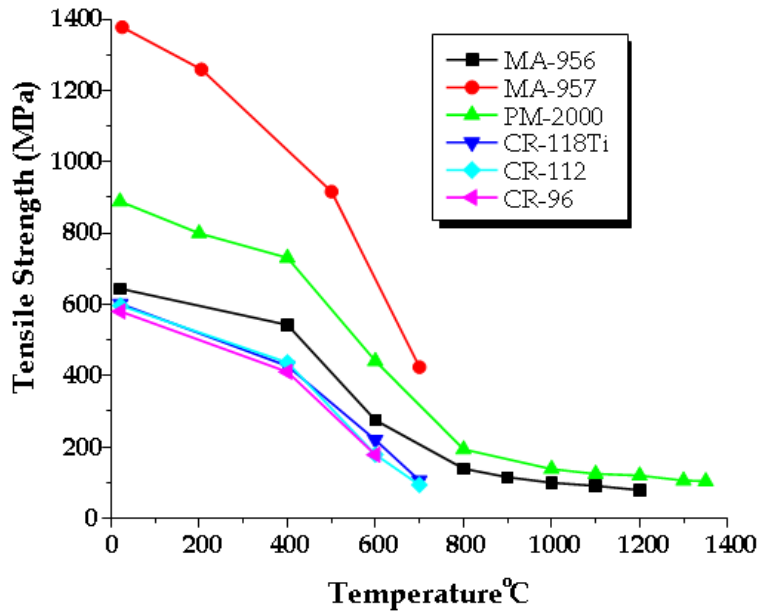
Figure 13. Elevated temperature tensile strength comparison of ferritic stainless steel ODS alloys.

The CR-alloys exhibited similar tensile strengths over the tested temperature range (21°C-700°C). The strength of the CR-alloys was found to be less than MA-956, MA-957, and PM 2000, but was most comparable to the strength of MA-956. It should also be noted that the strength of all the alloys seemed to converge above 700°C. Also, the ultimate tensile strength of the commercial alloys is not typically reported in the (weakest) transverse direction due to sample geometry constraints. If this data were available, the tensile strength results of the CR-alloys probably would be more comparable.

Failure analysis of the CR-alloys was conducted to evaluate how the microstructure had affected the tensile strength of the alloys. The fracture surfaces of failed room temperature tensile bars were analyzed using SEM with secondary electron imaging (SEI), and a longitudinal cross-section of each failed tensile bars was analyzed using SEM with BEI (Figure 14). Microstructure analysis indicates that failure was due to micro-void formation and coalescence that resulted from de-bonding of the matrix from residual non-ideal phases (i.e., $Fe_{17}Y_2$ or PPB oxide). The surface fracture analysis of alloy CR-96 found $Fe_{17}Y_2$ particles at the base of the micro-void dimples and cross-sectional analysis clearly showed de-bonding of the matrix from the $Fe_{17}Y_2$ particles. The surface fracture analysis of alloys CR-112 and CR-118 found "river lines" signifying that micro-crack formation occurred along residual PPB oxide, while cross-sectional fracture analysis of the two alloys illustrates the alignment of the PPB oxide with surface crack initiation sites.
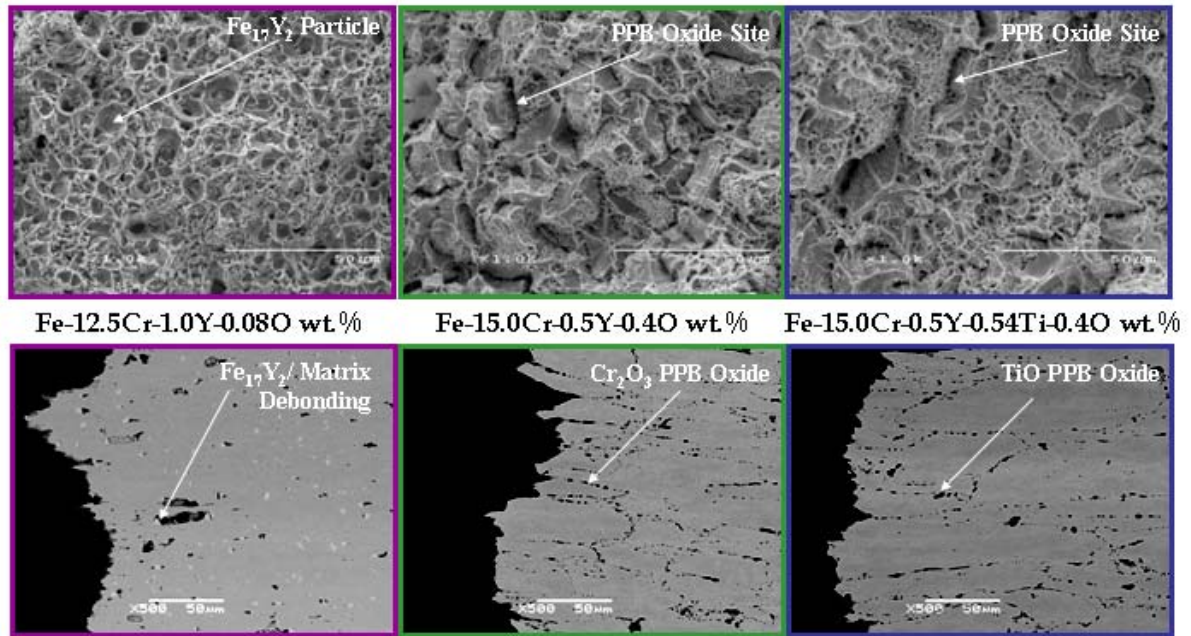
Figure 14. Surface and cross-sectional failure analysis of fractured tensile bar specimens CR-96 (purple), CR-112 (green), and CR-118 (blue).

The microstructure of the fractured tensile specimens was evaluated using bright field transmission electron microscopy (TEM), as displayed in Fig. 15.
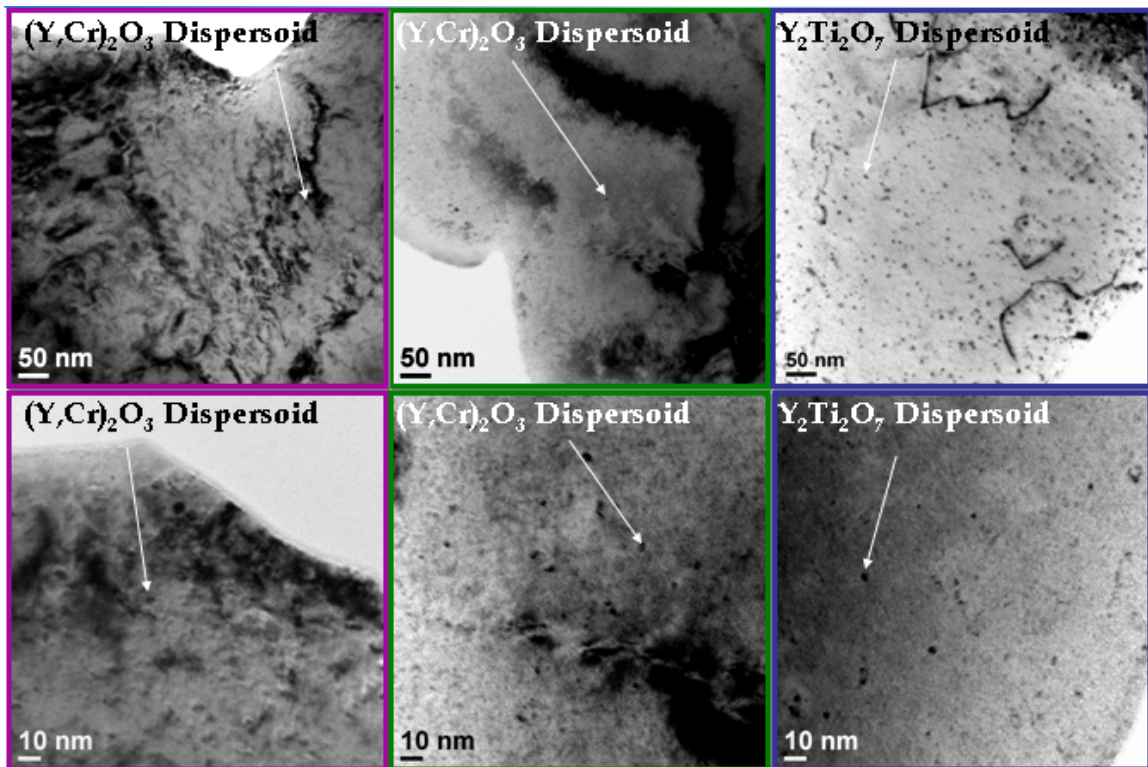

Figure 15. Microstructure evaluation of room temperature tensile bar specimens CR-96 (purple), CR-112 (green), and CR-118 (blue).

The analysis was conducted to evaluate the effective potential of forming nano-metric dispersoids during elevated temperature consolidation (i.e., 1300°C HIP) of precursor as-atomized powder particles. The microstructure of fractured room temperature tensile bar specimens is displayed in Figure 15. TEM analysis of all the CR-alloys confirms the formation of nano-metric yttrium enriched oxide dispersoids. The dispersoids identified in alloy CR-96 were typically less than 10nm in diameter and seemed to have a spherical morphology. The amount of dispersoids observed in alloy CR-96 was significantly less than the amount observed in alloys CR-112 and CR-118. The dispersoids identified in alloy CR-112 were generally less than 10nm in diameter and exhibited an apparent spherical morphology. Alloy CR-118 contained the most ideal nano-structure when comparing the three CR-alloys. The CR-118 microstructure contained a large number of yttrium-enriched dispersoids. The dispersoids appeared closely spaced (i.e., less than 20nm apart), were mostly less than 10nm in diameter, and had an apparent spherical morphology.

It should be noted that the initial tensile strengths of the CR-alloys were tested in the as-consolidated (i.e., 1300°C HIP) condition, without any attempt to optimize the heat treatment. The CR-alloys exhibited similar tensile strengths that seemed to be related to the similar deficiencies in each alloy microstructure, i.e., an equivalent residual non-ideal (i.e., $Fe_{17}Y_2$ or PPB oxide) phase fraction. During fracture analysis of the failed specimens, it was determined that the primary cause of failure occurred from debonding of the matrix from the non-ideal phases. On the other hand, the initial TEM results showed that the CR-alloys have the potential to form an ODS nano-structure with yttrium enriched dispersoids that are evenly distributed and of a size that is typically less than 10nm in diameter. Thus, the strength of the CR-alloys is expected to increase drastically once an ideal microstructure can be achieved, permitting a test of the true effectiveness of the dispersoids as precipitation strengtheners.

CONCLUSIONS

Modified sintering conditions and an innovative sample configuration were developed to produce a near-optimum (smooth, crack-free) porous membrane support surface by partial sintering of a loose layer of <3µm spherical gas atomized Fe-16Al-2Cr powders. The developments included a chamfered edge for the support tube to suppress rim (circumferential) cracking and a secondary support frit with approximately 10µm pore size to eliminate "sink hole" defects in the membrane support. Preserving a flat frit surface that matches with the chamfer edge seems to provide an ideal "glide surface" for sintering shrinkage of the powder layer, critical for avoiding surface cracking. Use of 316L stainless steel appeared superior to Inconel 600 for the frit to avoid a strong bonding reaction at the powder/frit interface. Tests of the completed hydrogen separation membrane system are needed to verify the effectiveness of an increased oxide diffusion barrier film at suppressing Fe and Cr diffusion into the Pd thin film.

A new simplified processing approach for ODS ferritic stainless steel was developed that involves gas atomization reaction synthesis (GARS) to produce a precursor "chemical reservoir" (CR) powder and full density isostatic powder consolidation to produce isotropic microstructures. During GARS, the powder particles are coated in situ with an oxide shell of a thickness controlled by the atomization parameters. That oxide shell is later dissociated and used as an oxygen reservoir during high temperature consolidation and heat treatment for the formation of evenly distributed nano-metric yttrium-enriched oxide dispersoids. The dissociation and formation reactions are driven by the thermodynamic stability hierarchy for the relevant oxides. It was demonstrated that there is a critical atomic ratio of yttrium to oxygen that must be satisfied to achieve an ideal microstructure, dependant on the composition of the final dispersoids. The initial tensile strengths of the CR-alloys were limited by the interfacial bond strength between the α-Fe matrix and residual non-ideal phases (i.e., $Fe_{17}Y_2$ or PPB oxide). The global microstructure

of CR-alloys needs improvement to ascertain the ideal strength of the alloy. The local nano-structure of the CR-alloys demonstrates that this process has great potential to effectively generate advanced ODS ferritic stainless steel alloys.

ACKNOWLEDGEMENTS

REFERENCES

1. R.L. Terpstra, I.E. Anderson, and B. Gleeson, "Porous Metallic Hot Gas Filters," *Advances in Powder Metallurgy and Particulate Materials-2003*, compiled by R. Lawcock and M. Wright, Metal Powder Industries Federation, Princeton, NJ, 2003, Part 9, pp. 73-85.
2. I.E. Anderson, R.L. Terpstra, J.A. Cronin, and R.S. Figliola, "Verification of Melt Property and Closed Wake Effects on Controlled Close-Coupled Gas Atomization Processes," in *Advances in Powder Metallurgy & Particulate Materials-2006*, compiled by W.R. Gasbarre and J.W. von Arx, Metal Powder Industries Federation, Princeton, NJ, 2006, part 2, pp. 1-16.
3. P. Tortorelli, et al., in *Proceedings of the 5th International Conference on Hot Gas Filtration*, NETL, Morgantown, WV, 2002, available at the USDOE website: www.netl.doe.gov.
4. S. Paglieri, in Conference Proceedings of 19th Annual Conference on Fossil Energy Materials, 2005, available at the USDOE website: www.netl.doe.gov.
5. I.E. Anderson, in Conference Proceedings of 21st Annual Conference on Fossil Energy Materials, 2007, available at the USDOE website: www.netl.doe.gov.
6. Z. Shi, S. Wu, and J.A. Szpunar, Appl. Phys. Lett., 87 (2005).
7. F. Roa, J.D. Way, R.L. McCormick, and S.N. Paglieri, Chem. Eng. J., 93(1)(2003), 11-22.
8. Y. Ma, B. Ceylan Akis, E. Ayturk, F. Guazzone, E. Engwall, and I. Mardilovich, Ind. Eng. Chem. Res, 43 (2004), 2936-2945.
9. R.L. Terpstra and I.E. Anderson, "Development of Thin Macro-Porous Metallic Support Structures for Hydrogen Separation Membranes," in *Advances in Powder Metallurgy & Particulate Materials-2005*, compiled by C. Ruas and T.A. Tomlin (Metal Powder Industries Federation, Princeton, NJ, 2005), Part 9, pp. 149-160.
10. I. E. Anderson, R.L. Terpstra, D.J. Byrd, and S.N. Paglieri, "Porous Metallic Support Structures Developed for Hydrogen Separation Membranes," in Advances in Powder Metallurgy and Particulate Materials-2008, compiled by R. Lawcock, A. Lawley, and P.J. McGeehan, (Metal Powder Industries Federation, Princeton, NJ, 2008), accepted.
11. S. Ukai, T. Nishida, and H. Okada, "Development of Oxide Dispersion Strengthened Ferritic Steels for FBR Core Application", *Journal of Nuclear Science and Technology*, 1997, vol. 34, no. 3, pp. 256-263.
12. S. Ukai, M. Harada, H. Okada, M. Inoue, S. Nomura, S. Shikakura, K. Asabe, T. Nishida, and M. Fujiwara, "Alloying design of oxide dispersion strengthened ferritic steel", *Journal of Nuclear Materials*, 1993, vol. 204, pp. 65-73.
13. S. Ukai, M. Harada, H. Okada, M. Inoue, S. Nomura, S. Shikakura, T. Nishida, M. Fujiwara, and K. Asabe, "Tube manufacturing and mechanical properties of oxide dispersion strengthened ferritic steel", *Journal of Nuclear Materials,* 1993, vol. 204, pp. 74-80.

14. D.T. Hoelzer, J. Bentley, M.A. Sokolov, M.K. Miller, G.R. Odette, and M.J. Alinger, "Influence of particle dispersions on the high-temperature strength of ferritic alloys", *Journal of Nuclear Materials*, 2007, 367-370, pp. 166-172.

15. G.R. Odette, M.J. Alinger, and B.D. Wirth, "Recent Development in Irradiation-Resistant Steels", *Annu. Rev. Mater. Res.,* 2008, vol. 38, no. 20, pp. 1-33.

16. J.F. Flumerfelt, and I.E. Anderson, "Gas Atomization Reaction Synthesis", *Processing Fabrication of Advanced Materials,* compiled by V.A. Ravi, T.S. Srivatsan, and J.J Moore, The Minerals, Metals, and Materials Society, Warrendale, Pa, 1994, vol. 3, pp. 475-486.

17. R. L. Terpstra, I. E. Anderson, F. Laabs, and J. R. Rieken, "Simplified Powder Processing of Oxide Dispersion Stainless Steel," in *Advances in Powder Metallurgy & Particulate Materials-2006*, compiled by W.R. Gasbarre and J.W. von Arx, Metal Powder Industries Federation, Princeton, NJ, 2006, part 9, pp. 1-14.

18. All materials processing was performed by the Materials Preparation Center of Ames Laboratory (USDOE). More information obtained from http://www.mpc.ameslab.gov/.

19. J. R. Rieken, I. E. Anderson, M. Kramer, Y. Wu, and M. Besser, "Atomized Precursor Alloy Powder for Oxide Dispersion Strengthened Ferritic Stainless Steel," in Advances in Powder Metallurgy and Particulate Materials-2008, compiled by R. Lawcock, A. Lawley, and P.J. McGeehan, (Metal Powder Industries Federation, Princeton, NJ, 2008), accepted.

20. M. Baster, F. Bouree, A. Kowalska, and Z. Latacz, J. Alloys Compds., 296, 1, 2000.

21. Natl. Bur. Stand. (U.S.) Monogram. 25, 19, 83, 1982.

22. Andersson, Acta Chem. Scand., 13, 415, 1959.

23. F. Molter, W. Eysel, Mineral-Petrograph. Institut der Universitat Heidelberg, Germany., ICDD Grant-in-Aid, 1991.

24. Engineering Data Sheet for Incoloy MA956, Special Metals Corp., SMC-008, October 2003.

25. M.L. Hamilton, D.S. Gelles, R.J. Lobsinger, G.D. Johnson, W.F. Brown, M.M. Paxton, R.J. Puigh, C.R. Eiholzer, C. Martinez, and M.A. Blotter, "Fabrication Technology Development of the Oxide Dispersion Strengthened Alloy MA957 for Fast Reactor Applications", Pacific Northwest National Laboratory, PNNL-13168, February 2000.

26. Materials Data Sheet ODS-Superalloy PM 2000, Metallwerk Plansee GmbH, February 1993.